RSC Advances

PAPER

View Article Online
View Journal | View Issue

Cite this: *RSC Adv.*, 2017, **7**, 19280

In situ DRIFT investigation on the photocatalytic NO oxidation mechanism with thermally exfoliated porous g-C_3N_4 nanosheets

Hong Wang,[a] Wenjie He,[a] Xing'an Dong,[a] Guangming Jiang,[a] Yuxin Zhang,[b] Yanjuan Sun*[a] and Fan Dong*[a]

Received 20th January 2017
Accepted 18th March 2017

DOI: 10.1039/c7ra00879a

rsc.li/rsc-advances

Bulk g-C_3N_4 suffers from a low surface area and high charge recombination rate. To advance the photocatalytic efficiency of g-C_3N_4, porous g-C_3N_4 nanosheets were prepared using a simple thermal exfoliation method. The effects of thermal exfoliation time on the microstructure and photocatalytic performance of g-C_3N_4 was investigated. Porous g-C_3N_4 nanosheets treated for 4 h (C_3N_4-4h) exhibited a highly enhanced NO removal ratio of 51.2%, which is 3.2 times higher than that of bulk g-C_3N_4. The enhanced activity of C_3N_4-4h can be ascribed to an increased surface area and promoted charge separation. An *in situ* DRIFT investigation was applied to monitor the time-dependent NO adsorption–photocatalysis process. Based on the observed reaction intermediates, a molecular-level mechanism for photocatalytic NO oxidation with porous g-C_3N_4 nanosheets was proposed.

1. Introduction

Graphitic carbon nitride (g-C_3N_4) as a stable and eco-friendly semiconducting photocatalyst, has attracted extensive attention due to its diverse potential applications in environmental remediation,[1] water splitting,[2] electrocatalysis[3,4] and water treatment.[5–7] However, the low specific surface area and the high recombination rate of charge carriers resulted in the relatively low visible light photocatalytic activity and thus limited its practical application.[8,9] In order to enhance the photocatalytic performance of g-C_3N_4, many strategies have been developed and applied. For instance, metal deposition,[10–14] metal/nonmetal doping,[15,16] coupling with other semiconductors,[17,18] and nanostructure engineering. Niu *et al.*[19] developed a thermal exfoliation method using for porous graphene-like g-C_3N_4 with enhanced photocatalytic activity. Dong *et al.*[20] investigated the effect of exfoliation temperature on the microstructure and photocatalytic performance of porous g-C_3N_4. It was found that the ultrathin exfoliated porous g-C_3N_4 nanosheets were favorable for charge transfer and reactants diffusion.

Recently, g-C_3N_4-based photocatalysts have been extensively reported the removal of NO. Dong *et al.*[21,22] immobilized the g-C_3N_4 photocatalysts on Al_2O_3 ceramic foam for efficient photocatalytic NO removal. The holes, superoxide and hydroxyl radicals were found to be the main reactive species for NO oxidation. Wang *et al.*[23] prepared g-C_3N_4 with honeycomb structures and applied them for enhanced photocatalytic NO removal. Li *et al.*[24] fabricated the g-C_3N_4/rutile-brookite $TiO_{2-x}N_y$ composite photocatalysts for NO purification. However, the mechanism of photocatalytic NO oxidation with g-C_3N_4 has not been revealed as the reaction intermediates during photocatalysis are difficult for to be detected. Also, the effects of thermal exfoliation time on the microstructure of porous g-C_3N_4 are still unknown.

Herein, we adopted the thermal exfoliation approach to prepare ultrathin porous g-C_3N_4 nanosheets. The effect of exfoliation time on the microstructure and photocatalytic performance of g-C_3N_4 investigated. The as-prepared porous g-C_3N_4 nanosheets were applied in visible light photocatalytic NO removal and exhibited enhanced activity. *In situ* DRIFT was employed to dynamically monitor the NO adsorption–photocatalysis process on the ultrathin porous g-C_3N_4 nanosheets. Based on the time-dependent evolution of reaction intermediates, a precise mechanism of photocatalytic NO oxidation was proposed. The present work could provide new insights into g-C_3N_4 photocatalysis mechanism for air purification.

2. Experimental

2.1 Synthesis of photocatalyst

2.1.1 Synthesis of g-C_3N_4. All chemicals were analytical grade purity and used without further purification. 0.50 g of dicyanodiamine was placed in an alumina crucible with a cover

[a]*Chongqing Key Laboratory of Catalysis and New Environmental Materials, Engineering Research Center for Waste Oil Recovery Technology and Equipment of Ministry of Education, College of Environment and Resources, Chongqing Technology and Business University, 400067 Chongqing, China. E-mail: syhsyj@163.com; dfctbu@126.com; Fax: +86-23-62769785-605; Tel: +86-23-62769785-605*

[b]*College of Materials Science and Engineering, National Key Laboratory of Fundamental Science of Micro/Nano-Devices and System Technology, Chongqing University, Chongqing 400044, China*

and calcined at 550 °C for 2 h with a ramping rate of 15 °C min^{-1}, and then cooled slowly to room temperature. The product was collected after grinding into powder in an agate mortar for further use.

2.1.2 Synthesis of reoxidized ultrathin g-C_3N_4. 0.5 g of the as-prepared g-C_3N_4 and 20 mL of deionized water were placed in an alumina crucible and calcined at 550 °C for different time (2, 4 and 6 h) with heating rate of 15 °C min^{-1} and then cooled slowly to room temperature. The product was collected as C_3N_4-2h, C_3N_4-4h, C_3N_4-6h after grinding.

2.2 Characterization

The prepared g-C_3N_4 samples were examined by XRD (XRD: model D/max RA, Japan). The morphology structures for the obtained products were characterized by transmission electron microscopy (TEM: JEM-2010, Japan). The optical absorption spectra were recorded on a UV-vis diffuse reflection spectrophotometer (UV-2450, Shimadzu, Japan) in the diffuse reflectance mode, using $BaSO_4$ as reflectance sample. The nitrogen adsorption–desorption isotherms were investigated in a nitrogen adsorption apparatus (ASAP 2020, USA) with products degassed at 150 °C prior to measurements. The photocurrent responses of the prepared samples were investigated in computer-controlled electrochemical apparatus.

2.3 Visible light photocatalytic activity

The photocatalytic activity of the obtained products was evaluated by oxidation of NO at ppb level in a continuous flow reactor. The volume of the rectangular reactor, made of stainless steel and covered with Saint-Glass, was 4.5 L (30 cm × 15 cm × 10 cm). A commercial tungsten halogen lamp (150 W) coupled with a 420 nm cutoff filter is utilized as the light source. For the test, 0.20 g of the photocatalyst spread on two sample dishes (12.0 cm in diameter) was placed in the middle of the reactor. By mixing with flowing air, the NO concentration is diluted to 600 ppb with a flow rate of 2.4 mL min^{-1} set by a mass flow controller. Then it was allowed to achieve an adsorption–desorption equilibrium. A NO_x analyzer was used to continuously measure the NO concentration during test. According to the equation $(\eta\%) = (1 - C/C_0) \times 100\%$ (C and C_0 represent the outlet and inlet NO concentrations, respectively), the NO removal rate (η) can be determined.

2.4 *In situ* DRIFTS study on photocatalytic NO oxidation process

In situ DRIFTS measurements were conducted using the Tensor II FTIR spectrometer (Bruker) equipped with an *in situ* diffuse reflectance cell (Harrick), as shown in Fig. 1. Photocatalysts were put into the cell. First, He gas (50 mL min^{-1}) was used to remove the residual hydrocarbons, H_2O and CO_2. The real-time FTIR spectrum after ventilation was utilized as background. Then, the reaction mixtures (25 mL min^{-1} NO, 25 mL min^{-1} O_2) were introduced into the cell. The NO adsorption on the catalysts was carried out for 20 min. Next, photocatalysts were illuminated by visible light source (MVL-210, Japan) for 40 min. The real-time FTIR spectra were detected every eight minutes.

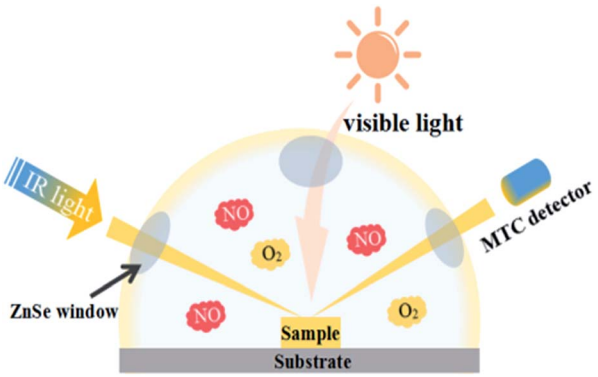

Fig. 1 Scheme of photoreaction cell used for *in situ* FT-IR data recording.

Meanwhile the gas fluxes keep the same (25 mL min^{-1} NO, 25 mL min^{-1} O_2). Finally, FTIR spectra were tested every two minutes with the same gas fluxes after turning off the light. The IR scanning range was 4000–600 cm^{-1} and 1900–1200 cm^{-1} was analyzed to present the photocatalytic oxidation process on porous g-C_3N_4 nanosheets.

3. Results and discussion

3.1 Crystal structures

Fig. 2 shows the XRD patterns of the prepared g-C_3N_4 samples treated for different time. All materials present two diffraction peaks, in agreement with the g-C_3N_4 (JCPDS card no. 87-1526), suggesting that the thermal treated g-C_3N_4 have similar crystal structure as their pristine bulk g-C_3N_4. The strong peak, identified as the (002) peak of graphitic materials, can be attributed to the characteristic inter-layer stacking of the conjugated aromatic C–N units.[25] This typical peak is shifted from 27.48° for C_3N_4 to 27.67° for C_3N_4-6h, which can be ascribed to the decreased inter-layer spacing due to thermal exfoliation effect. Another low-angle reflection peak is found around 13.1°, which is assigned to (100) peak and corresponds to an inter-planar distance of d = 0.68 nm from the in-plane structural stacking

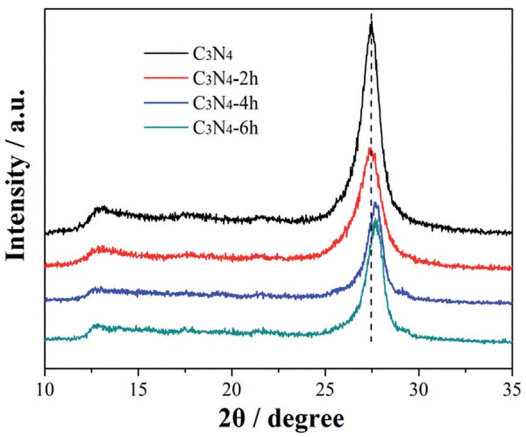

Fig. 2 XRD patterns of the C_3N_4, C_3N_4-2h, C_3N_4-4h and C_3N_4-6h.

motif.[25] Further, the (100) peak of C_3N_4-4h and C_3N_4-6h shifts to a lower angle of 12.7°, demonstrating that the planar size is increased during thermal exfoliation.[26]

3.2 Morphological structures

The morphology of the samples treated at different time was analyzed by TEM as showed in Fig. 3. Fig. 3a shows that the bulk C_3N_4 has a bulk layered structure. The enlarged view in Fig. 3b shows that the bulk C_3N_4 exhibits orderly stacked layers and a typical nonporous architecture. Compared to the pristine bulk g-C_3N_4 samples, the thermally treated g-C_3N_4 samples appear as thin and porous structure (Fig. 3c to h). This can be understood as the pristine bulk g-C_3N_4 samples were exfoliated into thin layers during thermal treatment. The bulk layered structure of g-C_3N_4 has typical CN layers linked together by weak van der Waals forces and hydrogen bonds. The van der Waals forces and hydrogen bonds are not stable enough against thermal oxidation process in air, and the layers of the CN unit would be gradually oxidized away from the bulk material in a layer-by-layer manner.[20] As showed in Fig. 3e to h, after thermal treatment for a long time, the C_3N_4-4h and C_3N_4-6h sample exhibit ultra-thin and porous layered structure. The AFM image (Fig. 4a) reflects that C_3N_4-4h has the nanosheets structure. As showed in Fig. 4b, the nanosheets thickness is 2.1 nm.

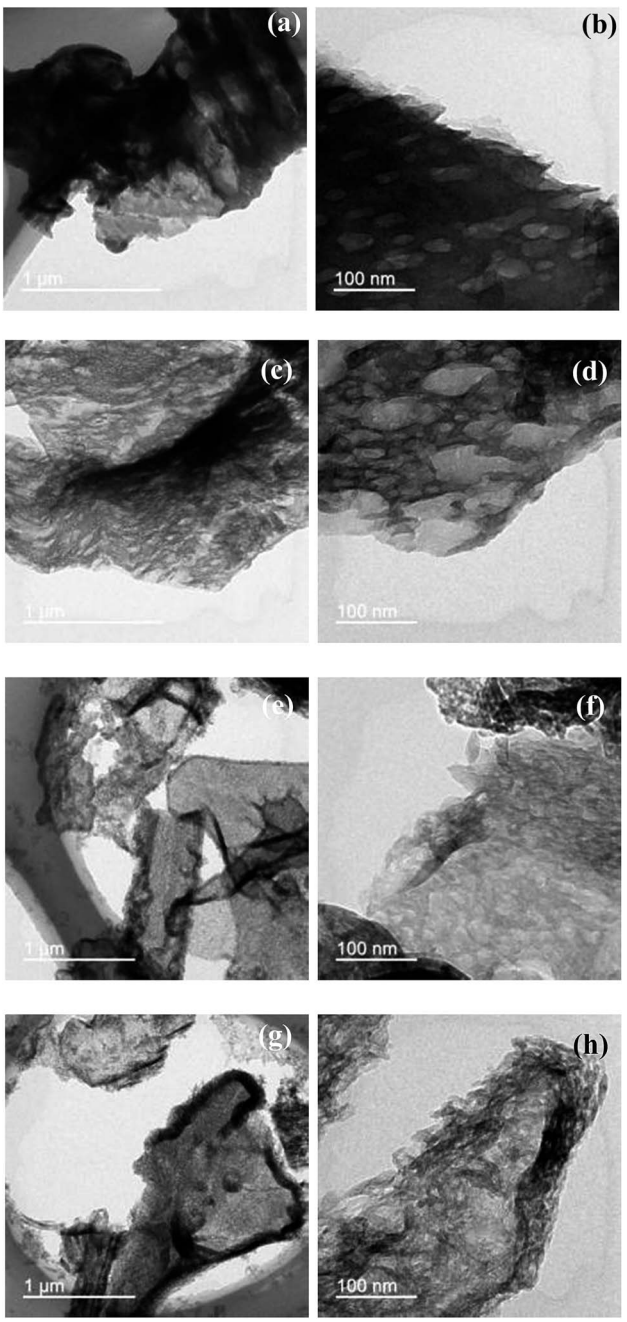

Fig. 3 TEM images of C_3N_4 (a, b), C_3N_4-2h (c, d), C_3N_4-4h (e, f) and C_3N_4-6h (g, h).

3.3 BET surface areas and pore structure

The detailed information about the specific surface areas and porosity of the C_3N_4, C_3N_4-2h, C_3N_4-4h and C_3N_4-6h was accessed by nitrogen absorption–desorption isotherms and Barrett–Joyner–Halenda (BJH) pore-size distribution are measured (Fig. 5 and Table 1). Fig. 5a shows that the above samples belong to type IV in BDDT classification shape of isotherms with a H3-type hysteresis loop in the IUPAC classification, suggesting the presence of slit-like mesopores. As showed in Fig. 5b, the C_3N_4-4h and C_3N_4-6h are abundant in large mesopores (22 to 60 nm) and small mesopores (3.79 nm).

The specific surface area, pore volume, peak pore size, and NO removal ratios are summarized in Table 1. The C_3N_4-4h has a higher specific surface area (122 $m^2\ g^{-1}$) and correspondingly larger pore volume (0.55 $cm^3\ g^{-1}$) than the others. Generally, the introduction of mesoporosity into g-C_3N_4 leads to increased

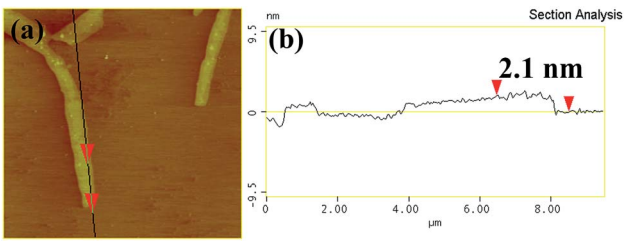

Fig. 4 The typical AFM image (a) and the corresponding thickness analysis results (b) of C_3N_4-4h.

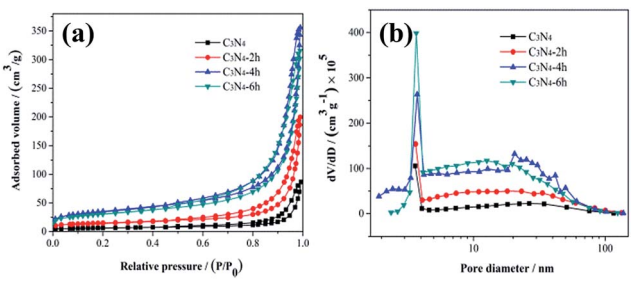

Fig. 5 N_2 adsorption–desorption isotherms (a) and the pore-size distribution curves (b) of the C_3N_4, C_3N_4-2h, C_3N_4-4h and C_3N_4-6h.

Table 1 The S_{BET}, total pore volume, peak pore size and NO removal ratio for C_3N_4, C_3N_4-2h, C_3N_4-4h and C_3N_4-6h

Sample name	S_{BET} ($m^2\ g^{-1}$)	Total pore volume ($cm^3\ g^{-1}$)	Peak pore size (nm)	NO removal ratio (%)
C_3N_4	20	0.13	3.6/26.5	16.0
C_3N_4-2h	50	0.31	3.6/18.0	47.8
C_3N_4-4h	122	0.55	3.7/20.5	51.2
C_3N_4-6h	105	0.49	3.6/12.6	49.7

surface areas.[20] The enlarged surface area would be beneficial for mass transfer and provide more active sites for photocatalysis reaction.[20]

3.4 Optical properties and band gap structure

As showed in the UV-vis DRS spectra (Fig. 6a), all the samples show an absorption edge (420–460 nm) in the visible light region. The absorption spectra of the samples thermal treated at different time exhibit an obvious blue shifted in comparison with the original g-C_3N_4. The band gap energy of C_3N_4, C_3N_4-2h, C_3N_4-4h and C_3N_4-6h are calculated to be 2.39, 2.46, 2.58 and 2.55 eV (Fig. 6b). The enlarged band gap for the thin layered samples can be attributed to the well-known quantum confinement effect by shifting the conduction and valence band edges in opposite directions.[27] The increase in band gap energy is beneficial for the enhancement of redox ability of the charge carriers generated by g-C_3N_4.

The separation efficiency of photogenerated carriers is investigated by the photocurrent measurement.[28] As shown in the wavelength-dependent photocurrent density in Fig. 7, in contrast to the pristine C_3N_4 with a low photocurrent density under visible-light irradiation, the C_3N_4-4h shows a remarkably improved photocurrent density, which indicates the enhanced charge separation efficiency of C_3N_4-4h sample. This could be attributed to ultra-thin layered structure of C_3N_4-4h sample (Fig. 3e and f), which could promote the charge migration and separation.[19,20]

3.5 Visible light photocatalytic activity and stability for NO removal

To demonstrate the photocatalytic activities of all the obtained samples for air purification, visible light photocatalytic removal

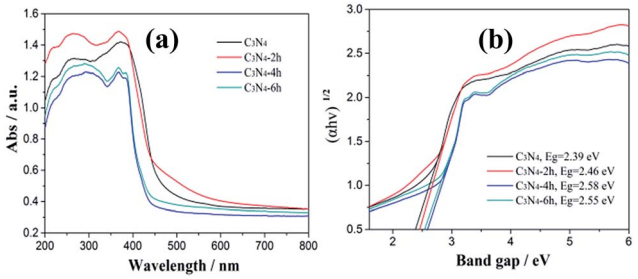

Fig. 6 UV-vis diffuse reflectance spectra (a) and band gap energies (b) of the C_3N_4, C_3N_4-2h, C_3N_4-4h and C_3N_4-6h.

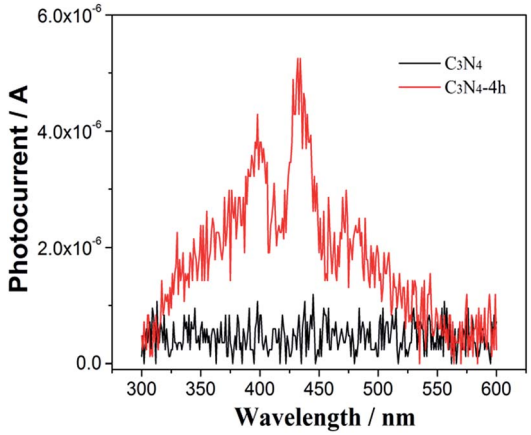

Fig. 7 Wavelength-dependent photocurrent of the C_3N_4, C_3N_4-2h, C_3N_4-4h and C_3N_4-6h.

of NO in air in a continuous reactor was carried out.[29–31] As showed in Fig. 8, the variation of NO concentration (C/C_0/%) with irradiation time over the g-C_3N_4 samples. After irradiation for 30 min, the NO removal ratio of the C_3N_4, C_3N_4-2h, C_3N_4-4h and C_3N_4-6h was 16.0%, 47.8% and 49.7%, respectively. Unprecedentedly, the C_3N_4-4h exhibited a dramatically enhanced NO removal ratio of 51.2%, 3.2 times higher than that of the bulk g-C_3N_4. The remarkably improved photocatalytic activities of the ultra-thin g-C_3N_4 demonstrated above can be explained as the synergistic effects of increased surface area and pore structure (Fig. 5b and Table 1), enhanced redox ability (Fig. 6b) and improvement in effective charge separation (Fig. 7).

The large surface area can increase the number of possible reactive sites for adsorption and diffusion of reactant molecules.[19] The ultra-thin layered structure of C_3N_4-4h could promote carrier transfer and separation and thus more carriers can take part in the photocatalytic reaction. The band gap of the C_3N_4-4h is increased by 0.2 eV, which could enhance the redox ability of charge carriers generated in the C_3N_4-4h. The significant role of a marginally increased band gap in promoting photo catalytic activities has also been reported from

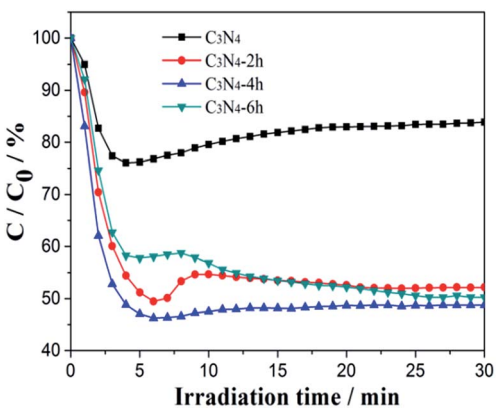

Fig. 8 Visible light photocatalytic activities of the C_3N_4, C_3N_4-2h, C_3N_4-4h and C_3N_4-6h.

$Cs_{0.68}Ti_{1.83}O_{4-x}N_x$ and faceted anatase TiO_2 crystals.[32–34] The above favorable factors co-contribute to the substantially improved photocatalytic activity of the ultra-thin g-C_3N_4.

3.6 *In situ* DRIFT study on the adsorption and photocatalytic NO reaction on g-C_3N_4 under visible light

3.6.1 NO adsorption and reaction on bulk g-C_3N_4. Fig. 9a shows the IR spectra of NO adsorbed on bulk g-C_3N_4. In the region of 900–1200 cm^{-1} and 3600–3750 cm^{-1}, several absorption bands were formed after the contact of bulk g-C_3N_4 with gaseous NO and O_2 at 25 °C. In the first 2 min, the adsorption of NO on bulk g-C_3N_4 resulted in the formation of iso-N_2O_4 (917 cm^{-1})[36] and N_2O (1121 cm^{-1}).[36] In the high-frequency region (3600–3750 cm^{-1}), plenty of adsorption bands can be observed after 4 min. All these bands (3604, 3623, 3635, 3663, 3683, 3696, 3717, 3729 and 3740 cm^{-1}) could attribute to NO_2.[36] Oxidation of NO with O_2 on bulk g-C_3N_4 caused the formation of NO_2. As time passed, the intensity of these bands is increased, as more amount of NO are adsorbed on bulk g-C_3N_4 and quickly transformed to NO_2. Especially, in the first 4 min, the adsorbed NO_2 may be consumed and transformed to N_2O_4, resulting in no obvious changes of spectra in the region of NO_2 (3600–3750 cm^{-1}).[37] Some investigators found that the band of N_2O increased at the beginning of NO adsorption and then decreased over time.[37] Noteworthy, similar results have been observed in this work. This may attribute to the NO of N–NO was further oxidation and formed NO_2, causing consumption of N_2O. The probable adsorption processes are proposed as follows (Table 2).[36,38]

$$NO + e_{(CN)}^- \rightarrow NO^- + e_{(CN)}^- \rightarrow NO^{2-}$$

$$NO + O_2 \rightarrow NO_2 \rightleftharpoons N_2O_4$$

$$NO + O_2 \rightarrow NO_3 + NO_2 \rightarrow N_2O_5$$

$$NO + NO_2 \rightarrow N_2O_3$$

$$NO + N_{(CN)} \rightarrow N_2O$$

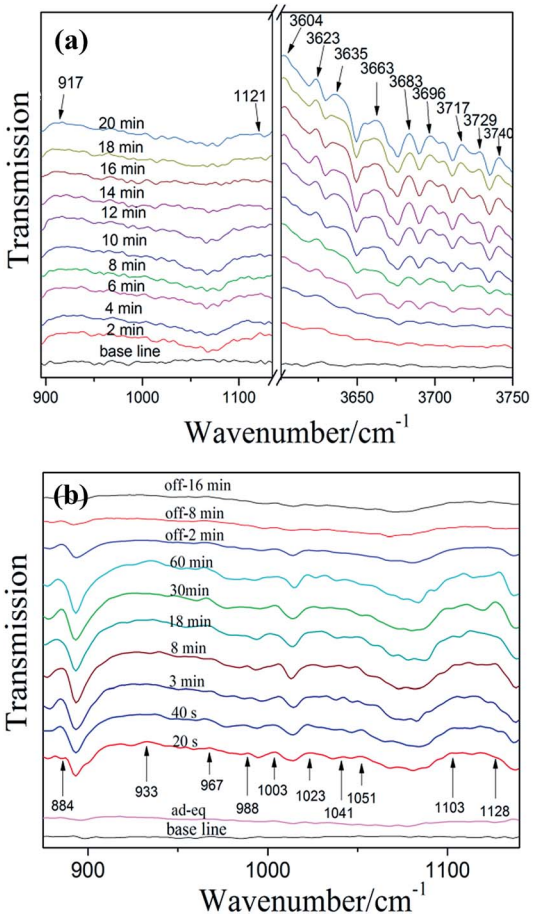

Fig. 9 *In situ* DRIFT spectra of adsorption (a) and photocatalytic reaction (b) on bulk g-C_3N_4 ("ad-eq" represents adsorption-equilibrium).

Fig. 9b shows the spectra of photocatalytic NO oxidation on bulk g-C_3N_4 during visible irradiation in time sequence. The spectrum of "ad-ep" is the same as that of "20 min" in Fig. 9a, at which NO and O_2 adsorption is reached equilibrium after introducing NO and O_2 in the dark. The irradiation with visible light for 20 s results in new absorption bands and causes significant changes in the region of 850–1150 cm^{-1}. Obviously, several new adsorption bands appear. These bands belong to reaction intermediates (NO^{2-}, N_2O_3 and NO^-) and final products (NO_2^- and NO_3^-). This indicates that some kinds of photogenerated active species induce the photocatalytic reaction and lead to the conversion of NO to intermediates and end products. According to previous work, the main reactive species for g-C_3N_4 are superoxide and hydroxyl radicals.[42] The absorption bands at 884, 967, 1103 and 1128 cm^{-1} can be indexed to NO^{2-}, N_2O_3, NO^- and N_2O, respectively.[36,41] The band at 933, 1003, 1023, 1041 and 1051 cm^{-1} can be assigned to nitrates (NO_3^-).[36,39,40] In addition, the NO_2^- was detected at 988 cm^{-1}.[39] Noteworthy, the peaks of formative species gradually disappear after visible-light off. However, we can see from the spectrum of "off-16 min", some weak adsorption peaks could be detected as some reaction species are still adsorbed on the surface of the photocatalyst.[22,43] The mechanism of photocatalytic NO

Table 2 Assignments of the FT-IR bands observed upon adsorption-reaction of NO on bulk g-C_3N_4 and C_3N_4-4h followed by visible irradiation

Wavenumbers (cm^{-1})	Assignment	References
884	NO^{2-}	36
933, 1003, 1009, 1023, 1041, 1051, 1002, 1038	NO^{3-}	36, 39 and 40
988	NO^{2-}	39
1099, 1103, 1113	NO^-/NOH	41
961, 967	*sym*-N^2O^3	36
1121, 1128, 1130	N_2O	
917, 914	iso-N_2O_4	
2821, 2881, 2945, 3463, 3603–3742	NO_2	
866, 902	N_2O_5	

oxidation reactions are proposed as follows ($NO_x = NO^{2-}$, N_2O_3, NO^- and N_2O).[22]

$$g\text{-}C_3N_4 + h\nu \rightarrow e^- + h^+$$

$$e^- + O_2 \rightarrow {}^{\cdot}O_2^-$$

$$O_2^- + 2H^+ + e^- \rightarrow H_2O_2$$

$$H_2O_2 + e^- \rightarrow {}^{\cdot}OH + OH^-$$

$$NO_x + {}^{\cdot}O_2^- \rightarrow NO_2^-/NO_3^-$$

$$2{}^{\cdot}OH + NO_x \rightarrow NO_2 + H_2O$$

$$NO_2 + {}^{\cdot}OH \rightarrow NO_2^-/NO_3^- + H^+$$

$$NO_2^- + {}^{\cdot}OH/{}^{\cdot}O_2^- \rightarrow NO_3^-$$

3.6.2 NO adsorption and reaction on exfoliated porous g-C_3N_4 nanosheets. Fig. 10a shows the spectra of NO adsorbed on exfoliated porous g-C_3N_4 nanosheets (C_3N_4-4h). The adsorption peaks in Fig. 9a appear in Fig. 10a as well. In addition, the new bands at 1009 and 1099 cm^{-1} were assigned to nitrates and NO^-.[36] Obviously, the bands assigned to NO_2 were appeared after 2 min, which indicates that C_3N_4-4h possess stronger adsorption ability than bulk g-C_3N_4. This could be attributed to the enlarged surface areas of C_3N_4-4h, which accelerate the absorption process and enhance the absorption of NO.

Fig. 10b shows the spectra photocatalytic NO oxidation on C_3N_4-4h during visible irradiation in time sequence. The new adsorption bands of reaction intermediates (NO_2 (at 2821, 2881, 2945 and 3463 cm^{-1}),[36] NOH (at 1113 cm^{-1}),[41] N_2O_5 (866 and 902 cm^{-1}),[36] N_2O_3 (961 cm^{-1})[36]) and final products nitrates (1002 and 1038 cm^{-1})[36,40] can be detected. The photocatalytic reaction process on bulk g-C_3N_4 and C_3N_4-4h exhibited similar behaviour and the mechanism was also applied to C_3N_4-4h. Obviously, the intensity of nitrate adsorption bands is stronger than the bulk g-C_3N_4. This indicates the C_3N_4-4h has higher photocatalytic oxidation ability, which leads to the production of more active species, promoting NO_x transformation from NO to final products of nitrates or nitrites.

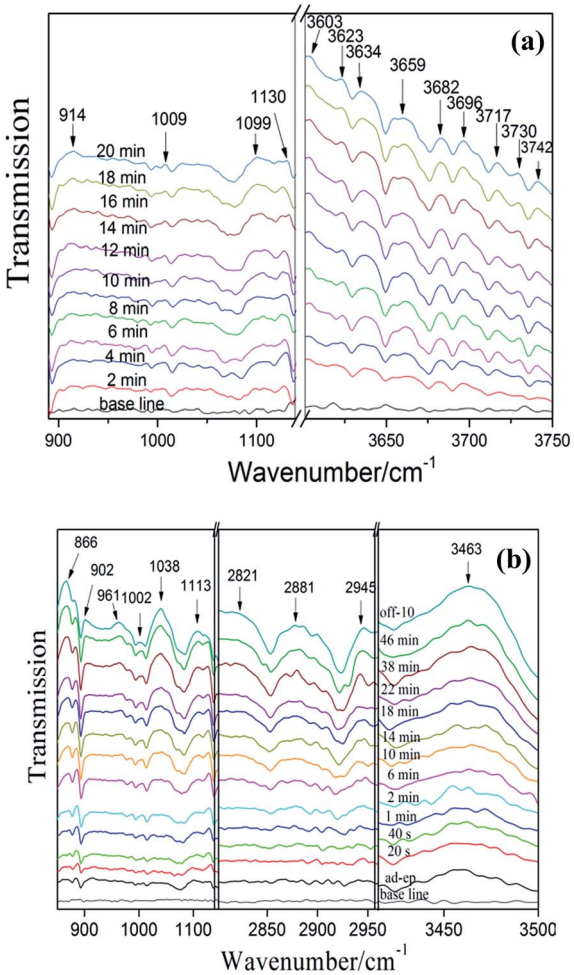

Fig. 10 *In situ* DRIFT spectra of adsorption (a) and photocatalytic reaction (b) on C_3N_4-4h.

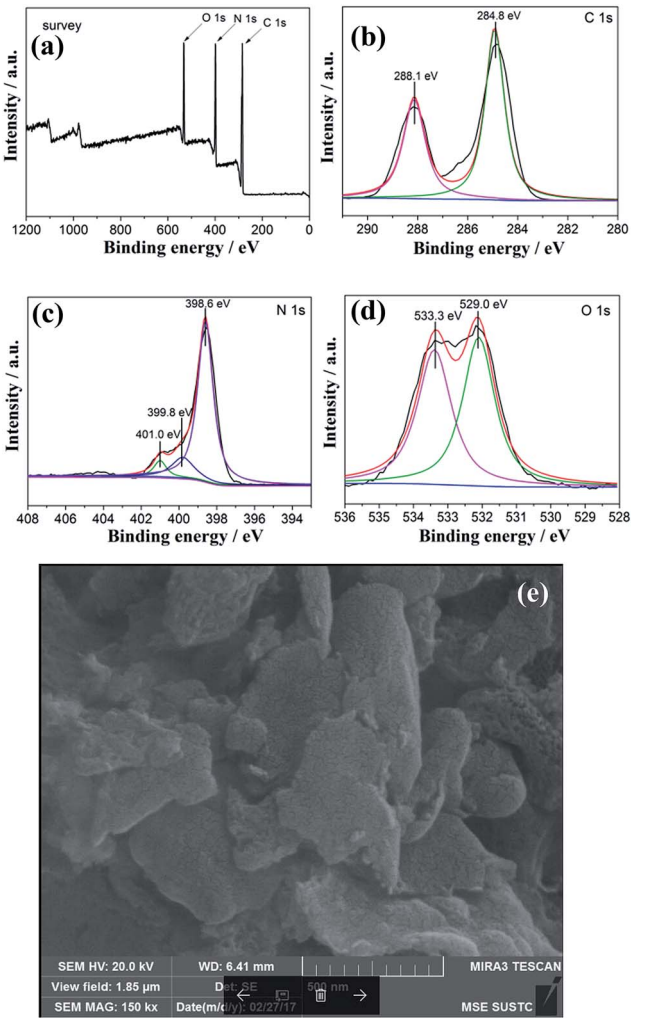

Fig. 11 XPS spectra of survey (a), C 1s (b), N 1s (c), O 1s (d) and SEM image (e) of C_3N_4-4h after recycled tests.

To determine the stability of the C_3N_4-4h, we carried out the XPS and SEM measurements of C_3N_4-4h after recycled photocatalytic test is shown in Fig. 11. The XPS measurements (Fig. 11a–d) show that the similar presence of C, N and O in the C_3N_4-4h after photocatalytic test.[35] Fig. 10 shows the typical high resolution XPS spectra for C, N and O elements, indicating that the chemical structure of C_3N_4-4h does not change after repeated irradiations. It can be observed from the SEM image (Fig. 11e) that the morphological structure of C_3N_4-4h is well-maintained.

4. Conclusions

In summary, the thermally treated ultra-thin porous g-C_3N_4 nanosheets were synthesized by a facile method. The porous g-C_3N_4 nanosheets exhibited remarkably enhanced photocatalytic activity in NO removal under visible light irradiation owing to the cooperation of the increased surface area and pore structure, enhanced redox ability and improvement of effective charge separation. The *in situ* DRIFT was employed to monitor the evolution of reaction intermediates basing on the time-dependent photocatalytic reaction. A mechanism for photocatalytic NO oxidation with g-C_3N_4 was proposed. The porous g-C_3N_4 nanosheets demonstrated enhanced adsorption performance and oxidation ability for NO. The present work could provide new insights into the understanding of g-C_3N_4 photocatalysis for NO removal.

Acknowledgements

This research was financially supported by National Natural Science Foundation of China (21501016, 51478070, 51108487 and 21676037), the Innovative Research Team of Chongqing (CXTDG201602014), Natural Science Foundation of Chongqing (cstc2016jcyjA0481 and cstc2015jcyjA0061), and the project from Chongqing Education Commission (KJ1600625, KJ1500601 and Kj1500637).

Notes and references

1 W. J. Ong, L. L. Tan, H. N. Yun, S. T. Yong and S. P. Chai, *Chem. Rev.*, 2016, **116**, 7159–7329.
2 G. Liu, P. Niu, C. Sun, S. C. Smith, Z. Chen, G. Q. Lu and H. M. Cheng, *J. Am. Chem. Soc.*, 2010, **132**, 11642–11648.
3 Y. Zheng, Y. Jiao, J. Chen, J. Liu, J. Liang, A. Du, W. Zhang, Z. Zhu, S. C. Smith and M. Jaroniec, *J. Am. Chem. Soc.*, 2011, **133**, 20116–20119.
4 J. Liang, Y. Zheng, J. Chen, J. Liu, D. Hulicova-Jurcakova, M. Jaroniec and S. Z. Qiao, *Angew. Chem., Int. Ed.*, 2012, **124**, 3958–3962.
5 S. Zhang, H. Gao, X. Liu, Y. S. Huang, X. Xu, N. S. Alharbi, T. Hayat and J. X. Li, *ACS Appl. Mater. Interfaces*, 2016, **8**, 35138–35149.
6 S. Zhang, J. Li, X. Wang, Y. Huang, M. Zeng and J. Xu, *ACS Appl. Mater. Interfaces*, 2014, **6**, 22116–22125.
7 S. Zhang, J. Li, X. Wang, Y. Huang, M. Zeng and J. Xu, *J. Mater. Chem. A*, 2015, **3**, 10119–10126.
8 S. Cao, J. Low, J. Yu and M. Jaroniec, *Adv. Mater.*, 2015, **46**, 2150–2176.
9 Q. Han, B. Wang, Y. Zhao, C. Hu and L. Qu, *Angew. Chem., Int. Ed.*, 2015, **54**, 11433–11437.
10 L. Yu, X. Zhang, C. Zhuang, L. Lin, R. Li and T. Peng, *Phys. Chem. Chem. Phys.*, 2014, **16**, 4106.
11 S. Samanta, S. Martha and K. Parida, *ChemCatChem*, 2014, **6**, 1453–1462.
12 X. Bai, R. Zong, C. Li, D. Liu, Y. Liu and Y. Zhu, *Appl. Catal., B*, 2014, **147**, 82–91.
13 O. Fontellescarceller, M. J. Mu ozbatista, M. Fernandezgarcia and A. Kubacka, *ACS Appl. Mater. Interfaces*, 2015, **6**, 22–25.
14 X. Wang, G. Zhang, Z. A. Lan, L. Lin and S. Lin, *Chem. Sci.*, 2016, **7**, 3062–3066.
15 Z. Ding, X. Chen, A. Markus and X. Wang, *ChemSusChem*, 2011, **4**, 274–281.
16 Z. Li, C. Kong and G. Lu, *J. Phys. Chem. C*, 2015, **120**, 56–63.
17 L. Gu, J. Wang, Z. Zou and X. Han, *J. Hazard. Mater.*, 2014, **268**, 216.
18 M. Xu, L. Han and S. Dong, *ACS Appl. Mater. Interfaces*, 2013, **5**, 12533–12540.
19 P. Niu, L. Zhang, G. Liu and H. M. Cheng, *Adv. Funct. Mater.*, 2012, **22**, 4763–4770.
20 F. Dong, Y. Li, Z. Wang and W. K. Ho, *Appl. Surf. Sci.*, 2015, **358**, 393–403.
21 Y. Sun, T. Xiong, Z. Ni, J. Liu, F. Dong, W. Zhang and W. K. Ho, *Appl. Surf. Sci.*, 2015, **358**, 356–362.
22 F. Dong, Z. Wang, Y. Li, W. K. Ho and S. C. Lee, *Environ. Sci. Technol.*, 2014, **48**, 10345–10353.
23 Z. Wang, W. Guan, Y. Sun, F. Dong, Y. Zhou and W. K. Ho, *Nanoscale*, 2015, **7**, 2471–2479.
24 H. Li, X. Wu, S. Yin, K. Katsumata and Y. Wang, *Appl. Surf. Sci.*, 2016, **392**, 531–539.
25 X. Wang, K. Maeda, A. Thomas, K. Takanabe, G. Xin, J. M. Carlsson, K. Domen and M. Antonietti, A metal-free polymeric photocatalyst for hydrogen production from water under visible light, *Nat. Mater.*, 2009, **8**, 76–80.
26 X. Yang, F. Qian, G. Zou, M. Li, J. Lu, Y. Li and M. Bao, *Appl. Catal., B*, 2016, **193**, 22–35.
27 A. P. Alivisatos, Semiconductor clusters, nanocrystals, and quantum dots, *Science*, 1996, **271**, 933–937.
28 H. G. Kim, P. H. Borse, W. Choi and J. S. Lee, *Angew. Chem.*, 2005, **44**, 4585–4589.
29 F. Dong, Z. Zhao, T. Xiong, Z. Ni, W. Zhang, Y. Sun and W. K. Ho, *ACS Appl. Mater. Interfaces*, 2013, **5**, 11392–11401.
30 T. Sano, S. Tsutsui, K. Koike, T. Hirakawa, Y. Teramoto, N. Negishi and K. Takeuchi, *J. Mater. Chem. A*, 2013, **1**, 6489–6496.
31 F. Dong, Z. Wang, Y. Sun, W. K. Ho and H. Zhang, *J. Colloid Interface Sci.*, 2013, **401**, 70–79.
32 G. Liu, P. Niu, L. Wang, G. Q. Lu and H. M. Cheng, *Catal. Sci. Technol.*, 2011, **1**, 222–225.
33 G. Liu, C. Sun, H. G. Yang, S. C. Smith, L. Wang, G. Q. Lu and H. M. Cheng, *Chem. Commun.*, 2010, **46**, 755–757.
34 J. Pan, G. Liu, G. Q. Lu and H. M. Cheng, *Angew. Chem., Int. Ed.*, 2011, **50**, 2133–2137.

35 C. Liu, Y. Zhang, F. Dong, X. Du and H. Huang, *J. Phys. Chem. C*, 2016, 10381–10389.
36 P. Jussieu, Characterization of Nitrogen Oxides by Vibrational Spectroscopy, *Inorg. Chem.*, 1982, 466–509.
37 J. C. S. Wu and Y. T. Cheng, *J. Catal.*, 2006, **237**, 393–404.
38 K. I. Hadjiivanov, *Catal. Rev.*, 2007, **42**(1&2), 71–144.
39 K. Hadjiivanov, V. Avreyska, A. Dimitar Klissurski and T. Marinova, *Langmuir*, 2002, **18**, 1619–1625.
40 T. Weingand, S. Kuba, K. Hadjiivanov and H. Knzinger, *J. Catal.*, 2002, **209**, 539–546.
41 M. Kantcheva, *J. Catal.*, 2001, **204**, 479–494.
42 W. Cui, X. Li, C. Gao, F. Dong and X. Chen, *Catal. Today*, 2016, 67–76.
43 Z. Zhao, Y. Sun, Q. Luo, F. Dong, H. Li and W. K. Ho, *Sci. Rep.*, 2015, **5**, 14643.